

Render unto Numerics: Orthogonal Polynomial Neural Operator for PDEs with Nonperiodic Boundary Conditions

Liu Ziyuan^a, Wang Haifeng^a, Bao Kaijun^a, Qian Xu ^{*a}, Zhang Hong^a, Song Songhe^{a,b}

^aCollege of Science, National University of Defense Technology, Changsha 410073, China

^bState Key Laboratory of High Performance Computing, National University of Defense Technology, Changsha 410073, China

Abstract

By learning the mappings between infinite function spaces using carefully designed neural networks, the operator learning methodology has exhibited significantly more efficiency than traditional methods in solving complex problems such as differential equations, but faces concerns about their accuracy and reliability. To overcome these limitations, combined with the structures of the spectral numerical method, a general neural architecture named spectral operator learning (SOL) is introduced, and one variant called the orthogonal polynomial neural operator (OPNO), developed for PDEs with Dirichlet, Neumann and Robin boundary conditions (BCs), is proposed later. The strict BC satisfaction properties and the universal approximation capacity of the OPNO are theoretically proven. A variety of numerical experiments with physical backgrounds show that the OPNO outperforms other existing deep learning methodologies, as well as the traditional 2nd-order finite difference method (FDM) with a considerably fine mesh (with the relative errors reaching the order of 10^{-6}), and is up to almost 5 magnitudes faster than the traditional method.

Keywords: deep learning-based PDE solver, neural operator, spectral method, AI4science, scientific machine learning.

2000 MSC: 47-08, 65D15, 65M22, 68Q32, 68T07

1. Introduction

Differential equations are the foundational models in numerous fields of modern science and engineering, and for decades, their solving processes have been dominated by numerical methods. However, recent research has shown that deep neural networks have an extraordinary capacity to solve highly nonlinear problems and the potential to develop algorithms more efficient than numerical methods. On the other hand, the stability and accuracy of numerical methods are ensured by numerical approximation theory, and these methods often lead to sparse systems, all of which are extremely desirable in the deployment of deep neural networks. Therefore, the following question arises: how can we incorporate these features to propose an innovative deep learning-based framework for partial differential equation (PDE) solvers?

Email address: qianxu@nudt.edu.cn (Qian Xu *)

In recent years, significant efforts have been oriented towards the development of deep learning-based PDE solvers. Some approaches focus on directly approximating PDE solutions with neural networks, such as the deep Galerkin method [25], the deep Ritz method [30, 11] and physically informed neural networks [21, 28] and are able to overcome the curse of dimensionality in theory but need retraining every time the PDE parameters or conditions are slightly changed. Furthermore, operator learning, a general methodology that learns the solution mappings between input and output function spaces, can efficiently generate the solution of an entire family of PDEs and is *roughly* categorized into two families of methods: FNO-like operators such as Fourier neural operators itself [33], the multiwavelet-based neural operator [5], the Galerkin transformer [2], spectral neural operators [3], and the integral autoencoder [19]; or DeepONet-like operators such as DeepONet [14], DeepM&Mnet [1], and MIONet [7]. Among the available operator learning methods, FNOs are both efficient and accurate and therefore may be the most fruitful and promising neural operator method to date for practical engineering applications, such as high-resolution weather forecasting [20], large-scale CO₂ injection simulations [4], subsurface two-phase oil/water flow simulations [31], and so on.

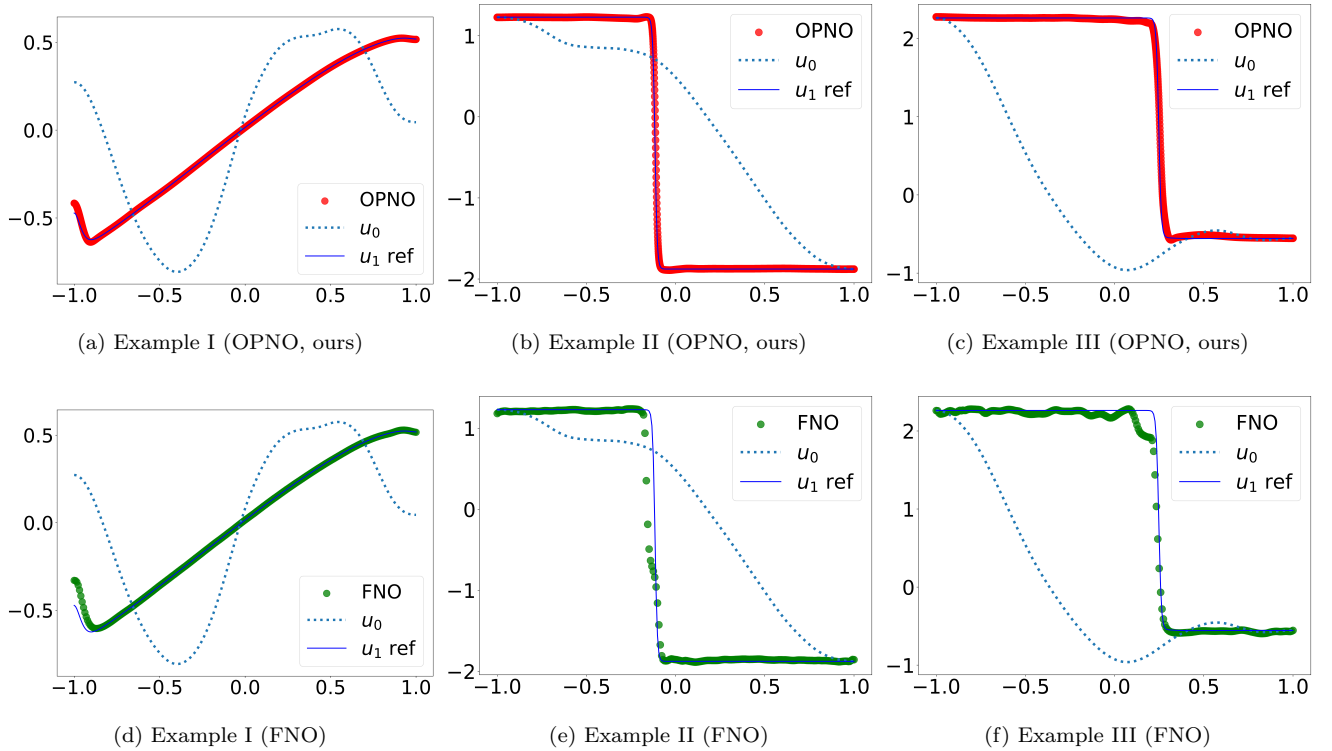


Figure 1: **Predictions of FNO model versus our OPNO for Burgers' equation with Neumann BCs.** The dotted and solid blue lines represent the initial condition $u_0(x)$ in the test dataset and the corresponding reference solution $u_1(x)$ when $t = 1$, respectively. The red dots in the upper figures are the predictions of our proposed OPNO method, while the green dots in the lower figures are their counterparts produced by the FNOs. Detailed discussions are presented in section 4.1.

While most neural operators are devoted to solving PDEs with periodic boundary conditions (BCs), limited

work has been done in cases with non-periodic BCs. More precisely, let $D \subset \mathbb{R}^d$ be a domain. We are interested in finding a θ -learnable-parameterized neural approximation \mathcal{G}_θ for the continuous operator

$$\mathcal{G} : \mathcal{A}(D; \mathbb{R}^{d_a}) \rightarrow \mathcal{U}(D; \mathbb{R}^{d_u}), \quad a \mapsto u \triangleq \mathcal{G}(a),$$

where $a \in \mathcal{A}(D; \mathbb{R}^{d_a})$ is an input function. When \mathcal{G} is the solution operators of PDEs, it is essential for \mathcal{G}_θ to precisely satisfy the imposed BCs. For example, consider the following time-dependent PDE with Neumann BCs:

$$\partial_t u(x, t) + \mathcal{N}(u) = 0, \quad x \in D,$$

subject to

$$\begin{aligned} u(x, 0) &= u_0(x), \quad x \in D, \\ \frac{\partial u}{\partial \mathbf{x}}(x, \cdot) &= 0, \quad x \in \partial D, \end{aligned} \tag{1}$$

and denote by $S(t)$ the solution operator that evolves the initial condition u_0 to the solution at time t , i.e.,

$$u(x, t) = S(t)u_0, \quad S(t + \delta t) = S(t)S(\delta t), \quad t, \delta t \geq 0.$$

If \mathcal{G}_θ is a numerical approximation of $S(1)$, the output $\mathcal{G}_\theta(u_0)$ should accurately satisfy the BCs in Eq. (1).

The three most common types of BCs in scientific and engineering computation are the Dirichlet BC

$$u(x, \cdot) = f(x), \quad x \in \partial D,$$

the Neumann BC

$$\frac{\partial u}{\partial \mathbf{n}} = g(x), \quad x \in \partial D,$$

and the Robin BC

$$au(x) + b \frac{\partial u}{\partial \mathbf{n}}(x) = h(x), \quad x \in \partial D,$$

which are known as the first-, second- and third-type boundary conditions, respectively. fig. 2 displays an example for these BCs.

Approaches for developing PINNs with hard constraints for non-periodic BCs or asymptotic limits were introduced in [17, 6, 13, 16, 10], where the neural networks needed to be retrained for different PDE parameters or initial conditions; thus, the direct generalization of these methods to neural operators seems ineffective. Besides, similar concept of preserving the properties of original system for deep-learning methods has been introduced in multiple papers by Pengzhan Jin, Yifa Tang, et al. [8, 32]. In Section 2, based on the neural network and spectral Galerkin methods [23, 24], we construct a general neural framework called spectral operator learning (SOL), and then in Section 3, we introduce an SOL method named the orthogonal polynomial neural operator (OPNO), which generates solutions satisfying the general BCs mentioned above **up to a machine precision limit**, as well as its universal approximation theorem. Moreover, the proposed method possesses the following appealing properties, which are also illustrated by numerical experiments in Section 4:

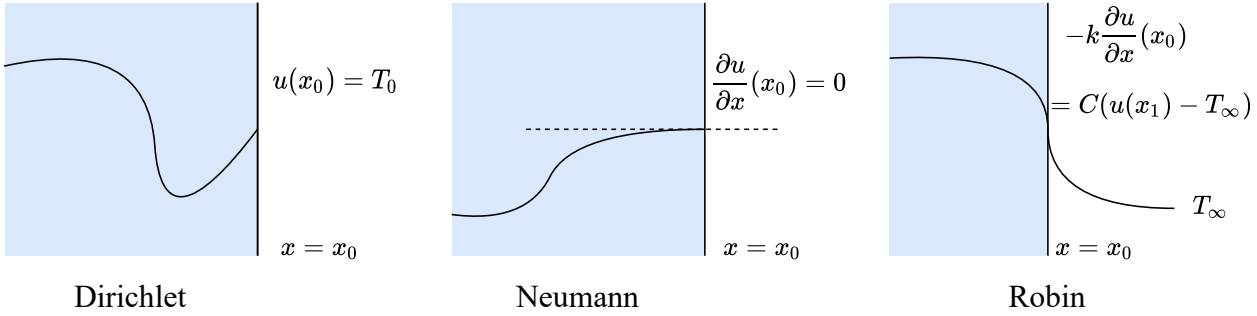


Figure 2: **An illustration of the three types of non-periodic BCs.** The heat diffusion equation is taken as an example, for which the solution $u(x)$ represents the temperature at point x . While the Dirichlet BC enforces a fixed temperature on the boundary, the Neumann BC describes an adiabatic or symmetric boundary effect by forcing the derivative to be zero, and the Robin BC, a linear combination of the two previous BCs, represents the heat convection between the heat source and the environment on the surface.

Quasi-linear computation complexity. The OPNO requires $O(N^d \log N)$ time complexity for d -dimensional problems due to the applications of the fast Chebyshev transform and the so-called fast compacting transform.

Efficient spatial differentiation computation. Since the output of the OPNO can be viewed as a polynomial function, its derivatives of arbitrary orders can be accurately computed within $O(N \log N)$ operations by the numerical method named differentiation in the frequency space (see appendix Appendix A). This approach avoids the vanishing gradient problem in the automatic differentiation of neural networks. In addition, readers may find that this property leads to a zero-shot learning methodology for solving PDEs, and this will be further investigated in our future work.

No overfitting during training. We have observed that as two typical examples of SOL, both the FNO and OPNO are well self-regularized when solving all the PDEs this paper involves, which means that their test errors do not obviously increase after extremely long-term training, even on a tiny training dataset. It is an extremely favorable feature for a deep learning method and suggests that an ultra-precise SOL method for specific PDEs is practically feasible.

Quasi-spectral accuracy. The spectral structure of the SOL approach leads to a behavior that is analogous to the spectral accuracy of spectral methods, which means that under the assumption of smoothness, a model trained on a coarse mesh can be directly applied to generate solutions on fine meshes without loss of numerical accuracy, and we presume that this is the reason for the observation of the “**resolution-invariant**” [33, 5, 2, 27] properties of some FNO-like methods.

Both of the code and dataset for the paper are available at https://github.com/liu-ziyuan-math/spectral_operator_learning.

2. Spectral Operator Learning

A general spectral neural operator \mathcal{G}_θ :

$\mathcal{A}(\Omega; \mathbb{R}^{d_a}) \rightarrow \mathcal{U}(\Omega; \mathbb{R}^{d_u})$, $a \mapsto G_\theta(a)$ is a mapping of the form

$$\mathcal{G}_\theta(a) = \mathcal{Q} \circ \mathcal{L}^{(L)} \circ \sigma \circ \mathcal{L}^{(L-1)} \circ \dots \circ \sigma \circ \mathcal{L}^{(1)} \circ \sigma \circ \mathcal{P}(a),$$

where σ is a non-polynomial activation function; $\mathcal{Q} : \mathcal{A}(D; \mathbb{R}^{d_a}) \rightarrow \mathcal{U}(D; \mathbb{R}^{d_v})$ and $\mathcal{P} : \mathcal{A}(D; \mathbb{R}^{d_v}) \rightarrow \mathcal{U}(D; \mathbb{R}^{d_u})$ are some simple structured neural networks; and $\mathcal{L}^{(l)}$ is a linear spectral operator layer of the form

$$\mathcal{L}^{(l)}(v) = \mathcal{T}^{-1}(A_l \cdot \mathcal{T}(v)). \quad (2)$$

In Eq. eq. (2), \mathcal{T} is a specific transformation operator that decomposes functions into the frequency domain

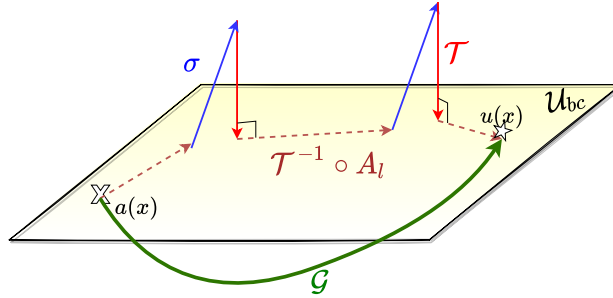


Figure 3: **Illustration of the architecture of SOL from the function space perspective.** Noting that \mathcal{T} is the projection to the function space of underlying basis that satisfy specific BCs, while $\mathcal{T}^{-1} \circ A_l$ is a linear transform on the space.

of the corresponding basis, for which the inverse operator is denoted by \mathcal{T}^{-1} , and $A_l \in \mathbb{R}^{d_v \times d_v}$ is a (learnable) parameterized linear transformation of the frequency domain. The idea of such an architecture was first introduced by Zongyi Li, Nikola Kovachki, et al. in the FNO [33], where $\mathcal{T} = \mathcal{F}$ (the Fourier transform) was considered, and A_l was fixed as a diagonal matrix:

$$(\mathcal{K}(\phi)v)(x) \triangleq \mathcal{F}^{-1}(\text{diag}(\Lambda) \cdot (\mathcal{F}v))(x). \quad (3)$$

Its significant associations with the numerical methods and the importance of choosing a correct basis, however, have not been fully discussed, which we find lead to a general framework of learning-based methods.

fig. 3 illustrates a sketch map for the SOL scheme. One can determine that the architecture of SOL alternately transforms the function **linearly** in the solution (frequency) space by a spectral operator and maps the function **nonlinearly** onto the physical space by an activation function. Readers may immediately discover the resemblance between SOL and the so-called pseudospectral techniques in numerical method, which numerically solves the **linear** part of a PDE with the spectral method in the frequency domain, while the **nonlinear** terms are solved in the physical space. Moreover, the spectral linear systems of SOL share the same pattern with their corresponding spectral methods (see fig. 4).

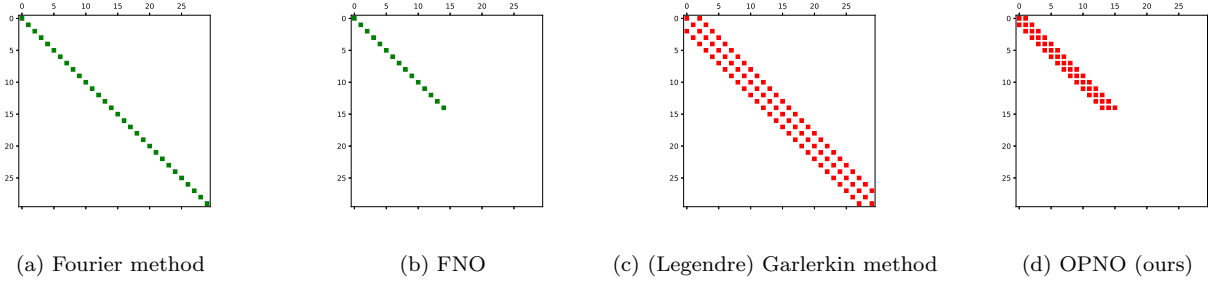


Figure 4: **Illustration for the sparse (spectral) linear systems** of the pseudospectral Fourier method (a), single-layer FNO (b), spectral Galerkin method (c) and single-layer OPNO (d), when solving the example boundary value problems $\Delta u + \alpha u = 0$, $\alpha \in \mathbb{R}$.

While the FNO is now widely applied in many problems with large scales and high complexity, most of the problems it has effectively solved are periodic, and we find that the performance of the FNO drops once the assumption of periodicity is not satisfied. For instance, [19] indicated that the FNO is not suitable for solving scattering problems with Sommerfeld radiation conditions. In addition, since the FNO is built on the truncated basis of trigonometric polynomials, the accuracy and computational stability may also be troubled with the so-called Gibbs phenomenon, which means that when applying Fourier methods to a non-periodic problem, spurious high-frequency oscillations will be generated near the boundaries, and the global convergence rate will be severely reduced (see fig. 5). It is common sense that for these kinds of PDEs, spectral methods with other bases, such as

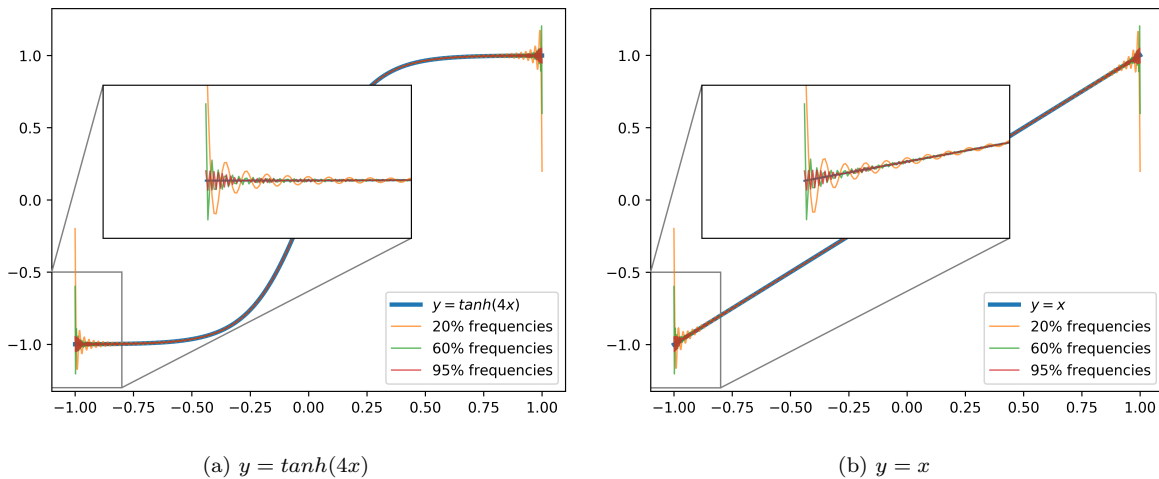


Figure 5: **The truncated Fourier expansions of non-periodic functions suffer from Gibbs phenomena.** The number of discretization points is set as $N = 1000$.

Chebyshev, Legendre and Hermite polynomials, should be applied rather than the Fourier spectral method [24].

Therefore, based on the spectral methods of orthogonal polynomials, especially of their compact combinations that will be introduced in section 3.2, we develop the OPNO to efficiently and reliably solve non-periodic PDEs

that are subject to the Dirichlet, Neumann, and Robin BCs. We focus on Chebyshev polynomials throughout this paper. The methodology, however, is also feasible for neural operators with other bases such as Legendre, Jacobi, Laguerre, Hermite polynomials, or spherical harmonic functions for specific problems, e.g., those on the cylindrical, spherical, or unbounded domain. However, such issues will not be addressed here. Furthermore, hybrid bases are useful for solving separable multi-dimensional problems or coupled equations with different BCs under the SOL framework.

3. The OPNO and its fast algorithm

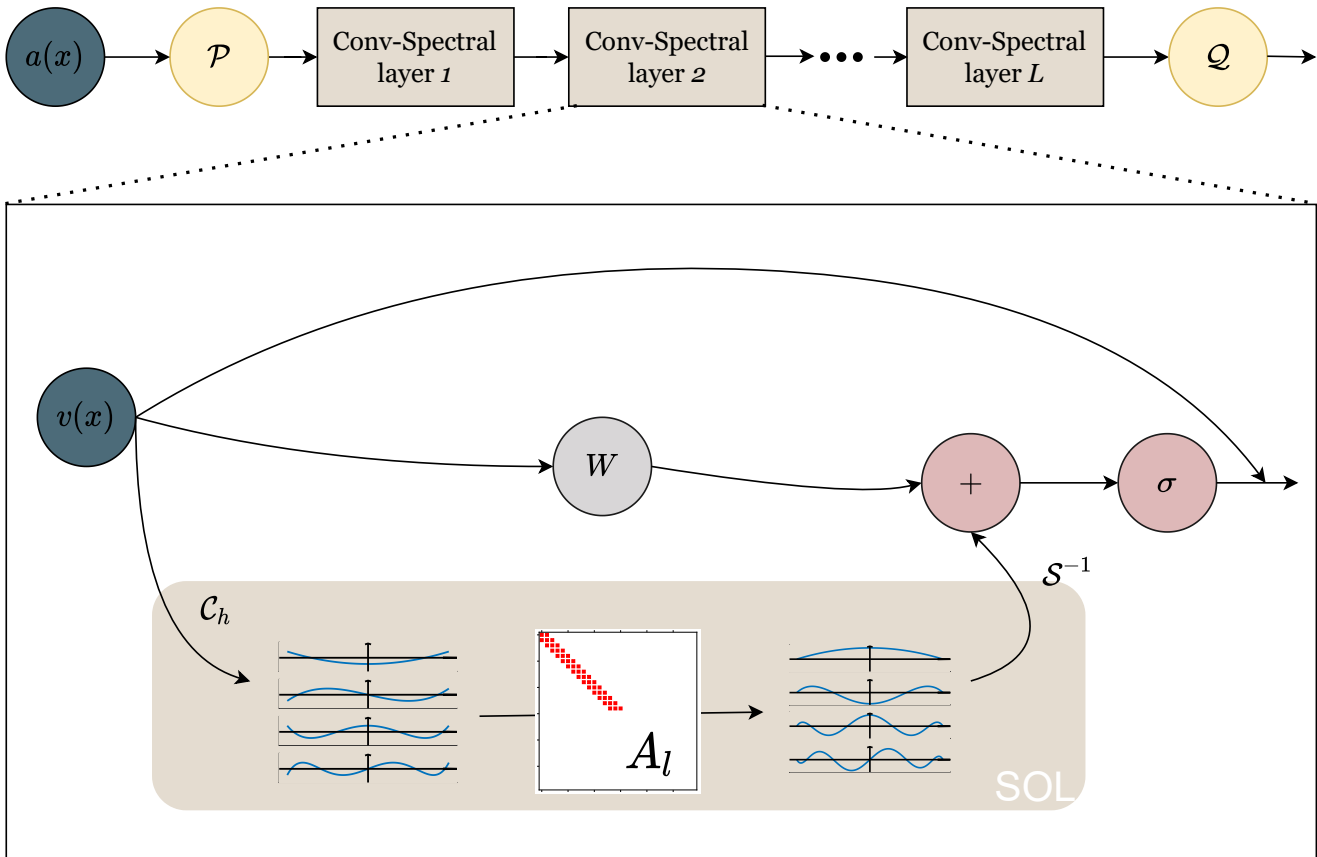


Figure 6: The architecture of the OPNO layers.

Without any loss of generalization, the interval $I = [-1, 1]$ is considered since the proposed method can be easily generalized to any interval $[a, b] \subset \mathbb{R}$ by a linear map such that

$$t = x(b - a)/2 + (a + b)/2, \quad t \in [a, b]$$

or to d -dimensional cases. Based on the compact combination basis of Chebyshev polynomials $\{\phi_k(x)\}$ that Jie Shen, Tao Tang and Li-lian Wang introduced in [24], we construct the fast Shen transform \mathcal{S} that maps an arbitrary function $u \in C(I)$ to its expansion coefficients on the compact combination basis. To fulfill this goal, the Shen

transform is split into the composition $\mathcal{S} = \mathcal{C}_p \circ \mathcal{C}_h$: the fast Chebyshev transform \mathcal{C}_h that maps the function into its Chebyshev coefficients is taken first ($x \rightarrow T_k$), and then the fast compacting transform \mathcal{C}_p mapping the Chebyshev coefficients to the coefficients of compact combinations ϕ_k ($T_k \rightarrow \phi_k$) follows.

3.1. Brief introduction to the fast Chebyshev transform \mathcal{C}_h

Chebyshev polynomials (of the first kind) $T_n(x)$ are a series of orthogonal polynomials given by the following three-term recurrence relation:

$$T_{n+1}(x) = 2xT_n(x) - T_{n-1}(x), \quad n \geq 1, \quad x \in I. \quad (4)$$

To list a few, $T_0(x) = 1$, $T_1(x) = x$, $T_2(x) = 2x^2 - 1$, and $T_3(x) = 4x^3 - 3x$. Denote $x_j = -\cos \frac{\pi j}{N}$, $0 \leq j \leq N$ as the Chebyshev-Gauss-Lobatto (CGL) points, and let $I_N u$ be the Lagrange interpolation polynomial relative to these CGL points; then, any function $u \in C(I)$ has a unique decomposition on the basis of T_k , namely,

$$(\Pi_N u)(x) = (I_N u)(x) \triangleq \sum_{n=0}^N \hat{u}_n T_n(x),$$

where $\Pi_N u$ denotes the Chebyshev decomposition transform and the Chebyshev coefficients $\{\hat{u}_n\}$ are determined by the (forward) discrete Chebyshev transform \mathcal{C}_h . The mathematical forms of \mathcal{C}_h and its inverse are listed below.

$$\hat{u}_n = \frac{2}{\tilde{c}_n N} \sum_{j=0}^N \frac{1}{\tilde{c}_j} u(x_j) \cos \frac{nj\pi}{N}, \quad 0 \leq n \leq N \quad (\text{forward transform}),$$

$$u(x_j) = \sum_{n=0}^N \hat{u}_n \cos \frac{nj\pi}{N}, \quad 0 \leq j \leq N \quad (\text{backward transform}),$$

where $\tilde{c}_0 = \tilde{c}_N = 2$ and $\tilde{c}_j = 1$ for $j = 1, 2, \dots, N-1$.

Moreover, the discrete Chebyshev transform and its inverse can be efficiently computed in $O(N \log N)$ operations via the fast cosine transform [26, 29]. A more detailed introduction is given in appendix Appendix A.

3.2. Compacting transform \mathcal{C}_p

As [24] introduced, the compact combination of Chebyshev polynomials $\{\phi_k(x)\}$ is a basis of polynomials that automatically satisfies specific BCs; this combination has the following form

$$\phi_i(x) = T_k(x) + a_k T_{k+1}(x) + b_k T_{k+2}(x).$$

More precisely, consider the general (Robin) BCs:

$$a_- u(-1) + b_- u'(-1) = 0, \quad a_+ u(1) + b_+ u'(1) = 0.$$

Then, there exists a unique set of $\{a_k, b_k\}$ such that $\phi_k(x)$ satisfies such conditions for all $k > 0$. It is remarkable that:

- For $a_{\pm} = 1$, $b_{\pm} = 0$ (Dirichlet BCs), we have $\phi_k(x) = T_k(x) - T_{k+2}(x)$.

- For $a_{\pm} = 0, b_{\pm} = 1$ (Neumann BCs), we have $\phi_k(x) = T_k(x) - \frac{k^2}{(k+2)^2}T_{k+2}(x)$.

The compacting transform \mathcal{C}_p maps the Chebyshev coefficients to the expansion coefficients on the ϕ_k of the same function. Notably, the compacting transform and its inverse are linear and can be carried out by recursion with $O(N)$ operations. For example, let $f = \sum_{j=0}^N \alpha_j T_j = \sum_{j=0}^{N-2} \beta_j \phi_j$, and consider the Dirichlet BCs such that $\phi_k = T_k - T_{k+2}$; then, we have the following:

forward compacting transform

$$\beta_j = \begin{cases} \alpha_j, & j = 0, 1, \\ \beta_{j-2} + \alpha_j, & 2 \leq j \leq N-4, \\ -\alpha_{j+2}, & j = N-3, N-2, \end{cases} \quad (5)$$

and **backward compacting transform**

$$\alpha_j = \begin{cases} \beta_j, & j = 0, 1, \\ \beta_j - \beta_{j-2}, & 2 \leq j \leq N-2, \\ -\beta_{j-2}, & j = N-1, N. \end{cases}$$

The forward and backward compacting transforms for cases with Neumann BCs are provided in appendix Appendix B.

3.2.1. Fast compacting transform

Although the native forward compacting transform theoretically costs $O(N)$ floating point operations (FLOPs), the coefficients need to be computed by recursion; thus, it is not suitable for computation on GPUs. Consequently, we propose a parallelable fast compacting transform. Suppose $N \geq 3$, and let \mathbf{s} be an $(N+1)$ -dimensional vector with elements

$$s_j = \begin{cases} 0, & j = 1, 3, 5, \dots, 2\lfloor N/2 \rfloor - 1, \\ 1, & j = 0, 2, 4, \dots, 2\lfloor N/2 \rfloor. \end{cases}$$

We usually ignore the special cases of $j \geq N-3$ in Eq. eq. (5) for simplicity or computational stability when the function $f = \sum_{j=0}^N \alpha_j T_j$ satisfies the corresponding BCs. Then one can see that Eq. eq. (5) is equivalent to the **linear convolution** of $\boldsymbol{\alpha}$ and \mathbf{s} , i.e.,

$$\beta_j = \sum_{k=0}^{\lfloor j/2 \rfloor} \alpha_{j-2k} = \sum_{k=0}^j \alpha_{j-k} s_k.$$

The fast algorithm for discrete linear convolution is alrigh highly developed and can be quickly given by the FFT algorithm, namely

$$\boldsymbol{\beta} = \mathcal{F}^{-1}(\mathcal{F}(\bar{\mathbf{s}}) \cdot \mathcal{F}(\bar{\boldsymbol{\alpha}})),$$

where the $\bar{\bullet}$ symbol represents zero-padding the vector to a length of $2N+2$ at its end (see fig. 7). The fast compacting transform exhibits approximately a threefold increase in speed in the numerical experiments.

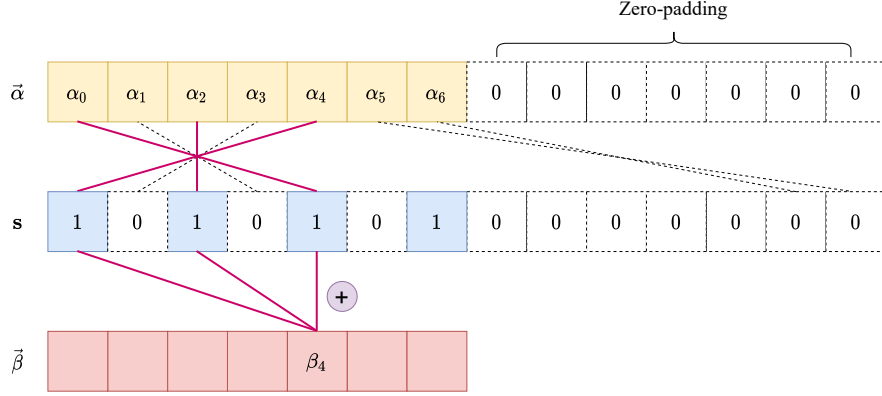


Figure 7: **Schematic diagram of the linear convolutions of fast compacting transform \mathcal{C}_p** when $N = 6$, so that $\mathbf{s} = (1, 0, 1, 0, 1, 0, 1)^T$ and $\beta_4 = \alpha_4 + \alpha_2 + \alpha_0$.

3.3. Structure of the OPNO

We finally come to the structure of the OPNO. The vanilla spectral kernel layer is first given by substituting \mathcal{T} in Eq. eq. (2) with the Shen transform $\mathcal{S} \triangleq \mathcal{C}_p \circ \mathcal{C}_h$, i.e.,

$$\tilde{\mathcal{L}}_{ker}^{(l)}(v) = \mathcal{S}^{-1}(A_l \cdot \mathcal{S}(v)).$$

In addition, as the linear system of the spectral Galerkin method implies (see fig. 4), A_l is a quasi-diagonal matrix with a bandwidth of w , and truncated to k modes to reduce the number of model parameters and focus on the low-frequency behavior of the target operator. We find that $w = 3$ suffices in all the numerical examples. In addition, out of consideration for efficiency, since \mathcal{C}_p is such a simple linear transform that can be easily learned, it is omitted in all forward Shen transform steps except in the final projection layer \mathcal{Q} . In total, a further 2X speed optimization is witnessed without noticeable accuracy loss. Therefore, the spectral kernel layer we implement is given by

$$\mathcal{L}_{ker}^{(l)}(v) = \mathcal{S}^{-1}(A_l \cdot \mathcal{C}_h(v)).$$

On top of that, there are some details worth mentioning. As we have emphasized before, it is significant for the outputs to accurately satisfy the BC, so the output of the OPNO is again projected onto the space of $\{\phi_k\}$ via the projection layer \mathcal{Q} ; namely,

$$\mathcal{Q}(v) = \mathcal{S}^{-1}[\mathbf{1}_{k \leq N} \mathcal{S}(Q(v))], \quad (6)$$

where Q is usually a shallow neural network. In fact, to prove the convergence properties of the FNO for periodic problems, [9] has introduced the same projection to FNOs on the space of trigonometric functions rather than the native σ -activated FNOs. We assume that the native FNO sacrifices the inherent periodic property for generalizations to non-periodic problems. As the output of the OPNO is a finite summation of underlying basis functions, the following BC satisfaction theorem holds.

Theorem 3.1 (BC satisfaction). *For any OPNO \mathcal{G}_θ with the projection operator \mathcal{Q} of the form Eq. eq. (6), and any $a \in H^s(I)$, the output $u = \mathcal{G}_\theta(a)$ satisfies the BCs of the underlying basis of \mathcal{G}_θ .*

Moreover, to capture the high-frequency part of the target operator, just as the FNO deployed, we also assemble a joint ‘‘Conv-Spectral’’ layer by adding an auxiliary linear neural layer W_l parallel to each $\mathcal{L}_{ker}^{(l)}$ layer. From the perspective of spaital dimension, such linear neural layers are Convolutional Neural Networks (CNN) with a 1×1 kernel; remark that they do not break the SOL-structure in fig. 3. The joint Conv-Spectral layers are the backbone of our model, and readers may also see a sketch map shown in fig. 6.

Finally, we find that the skipping-connection skill of ResNet may slightly improve the resulting performance. To prevent the lifting operator \mathcal{P} from interrupting the skipping structure, \mathcal{P} is implemeted as a dense block of the input function and a kernel layer.

In summary, the architecture of the OPNO layer is demonstrated as follows,

$$v^{(l+1)} = v^{(l)} + \sigma(W_l v^{(l)} + b_l + \mathcal{S}^{-1}(A_l \cdot \mathcal{C}_h(v^{(l)}))). \quad (7)$$

The OPNO also satisfies the following universal approximation theorem, and the associated proof is provided in appendix Appendix C.

Theorem 3.2 (Universal Approximation Theorem). *Let $s \geq 0$ and let $\mathcal{G} : H^s(I^d; \mathbb{R}^{d_a}) \rightarrow L^2(I^d; \mathbb{R}^{d_u})$ be a continuous operator. Consider $K \subset H^s(I^d; \mathbb{R}^{d_a})$ a compact subset; then, $\forall \epsilon > 0$, there exists an OPNO $\mathcal{L} : H^s(I^d; \mathbb{R}^{d_a}) \rightarrow L^2(I^d; \mathbb{R}^{d_u})$ such that*

$$\|\mathcal{L}(a) - \mathcal{G}(a)\|_{L^2} < \epsilon, \quad \forall a \in K.$$

4. Numerical Experiments

To verify the accuracy and computational features (quasi-linear computational complexity, self-regularization, resolution-invariant error, etc.) of the OPNO, we compare it with four popular neural operator models and the finite difference method (FDM) in terms of solving four PDEs: (1) Burgers’ equation with Neumann BCs; (2) the heat diffusion equation with Robin BCs; (3) the heat diffusion equation with inhomogeneous Dirichlet BCs; and (4) the 2D Burgers’ equation. The accuracy of the models is measured by the average relative L^2 norm error between the predicted solution and the reference solutions, which are given by Chebyshev spectral methods, as well as the L^∞ norm error on the corresponding BCs. The four baseline deep learning models are listed below.

1. **FNO** is a state-of-the-art neural operator for solving parametric PDEs [33]. The original paper also presented a series of methods for generating supervised training datasets for the learning-based PDE solvers, which are now cited as classic datasets in multiple papers.
2. **Galerkin transformer** (GT) [2], a self-attention-based neural operator that introduces a novel linear and softmax-free attention mechanism, has wide applications in both PDE solving and pattern recognition.
3. **IAE-Net** [19], a neural operator that consists of an encoder-decoder structure and integral transforms, has surpassed various models in solving PDEs and performing signal/image processing in experiments, especially those with non-periodic BCs such as radiation BCs.

4. **POD-DeepONet** (POD-DO) [15] is an improved DeepONet model based on the proper orthogonal decomposition (POD) basis and is used for comparison with FNO in the paper. The DeepONet model is acknowledged for its computational efficiency and geometric flexibility. It also has a solid theoretical foundation due to its streamlined branch-trunk structures.

To eliminate the impact of different neural network training techniques, the hyperparameters of different models are selected to be the same, or consistent with those in their original papers, whereas the number of training epochs and decay step size of the learning rate simply increase to 5000 and 500, respectively, to ensure that all models are well trained (see table 1). The learnable parameters of all models are in double-precision format ('float64' or 'complex128').

Table 1: **Default settings of the deep learning methods:** batch sizes (bs), numbers of training epochs, training optimizers, spectral modes, spectral channel widths, numbers of Conv-Spectral layers (L), types of interpolation grids, and activation functions. The parameters *in italics* vary from their original papers and open-source code. Note that a single FNO mode actually consists of **two** trigonometric polynomials and is indicated by "(C)".

Hyperparameter	bs	epochs	optimizer	modes	width	L	grids	σ
FNO	20	<i>5000</i>	ADAM	<i>20(C)</i>	<i>50</i>	4	Uniform	GeLU
OPNO	20	5000	ADAM	40	50	4	CGL	GeLU
IAE	50	<i>5000</i>	ADAM	256	64	4	Uniform	ReLU
GT	4	<i>5000</i>	1cycle	<i>20(C)</i>	<i>50</i>	4	Uniform	ReLU
POD-DO	20	500000	ADAM	32	–	–	Uniform	tanh

4.1. Experiment 1: Viscous Burgers equation with Neumann BCs

We consider the one-dimensional viscous Burgers equation

$$\partial_t u(x, t) + \frac{1}{2} \partial_x (u^2(x, t)) = \nu \partial_{xx} u(x, t), \quad x \in I \quad (8)$$

subject to the initial-boundary conditions

$$u(x, 0) = u_0(x), \quad (9)$$

$$\frac{\partial u}{\partial x}(\pm 1, t) = 0, \quad t > 0, \quad (10)$$

and we aim to learn the solution operator $S(1) : S(1)u_0 \mapsto u(\cdot, 1), u_0 \in H^s(I)$. Burgers' equation is an important PDE in various fields, such as fluid dynamics, traffic flow and shock wave theory, while the Neumann BC represents the free flow of fluid in/out of the boundary and is quite common in its modeling scenarios. The initial condition $u_0(x)$ is generated using a Gaussian random field according to $u_0 \sim \mu$, where $\mu = \mathcal{N}(0, 625(-4\Delta + 25I)^{-2})$ with Neumann BCs, its Karhunen–Loève (K–L) expansion being of the form

$$u_0(x) = \sum_{k=0}^{\infty} 25(4(k\pi/2)^2 + 25)^{-1} \cdot \text{Re} \left\{ e^{ik\pi x/2} \right\} \cdot \xi_k, \quad x \in [-1, 1], \quad (11)$$

where $\{\xi\}_k$ are i.i.d. standard Gaussian random variables. In addition, the viscosity is set as $\nu = 0.1/\pi$; then, 1000 instances are generated for training as well as 100 instances for test. Therefore, except for the effect of different BCs, such a dataset has almost the same pattern as that of the FNO dataset for Burgers’ equation with the periodic BC in [33], and we can assert that such a comparison is fair.

The global relative L^2 error and the L^∞ error of the BCs are shown in table 2, where the L^∞ norm BC error for CGL grid outputs is computed by the polynomial differentiation method eq. (A.2), and those for uniform grid outputs are approximated by the first-order difference; i.e., let $h = \frac{2}{N}$ denotes the spatial step size, then

$$\mathcal{E}_{b.c.L^\infty} = \max \{|\delta_x u_0|, |\delta_x u_{N-1}|\},$$

where

$$\delta_x u_n \triangleq \frac{u_{n+1} - u_n}{h}$$

From the results, we can deduce the following conclusion.

- As table 2 shows, The OPNO outperforms other models not only in terms of the BC accuracy but also in terms of the global precision. Further evidence is shown in fig. 1 that the OPNO generate predictions that are “globally accurate”.
- It is shown in fig. 9 that the higher average errors of non-BC-satisfying models result from the bad performance on a handful of “hard” samples, which implies the OPNO is more reliable in terms of the worst-case performance due to the BC satisfaction property.
- fig. 8a illustrates that the test errors of FNO, OPNO, GT, and IAE-Net do not increase after long-term training, so these models possess the self-regulation properties when solving the PDEs we are interested in, and the decision of extending the number of training epochs successfully improved their performance by mitigating underfitting. Other experiments **also** follow the same non-overfitting pattern, see fig. 8b for an example.

Table 2: Benchmarks on 1D Burgers equation with Neumann BCs

N	256		1024		4096	
	L^2	b.c. L^∞	L^2	b.c. L^∞	L^2	b.c. L^∞
FNO	$1.571e - 2$	$2.902e - 1$	$1.684e - 2$	$4.092e - 1$	$1.688e - 2$	$5.478e - 1$
OPNO	$7.704e - 3$	$5.963e - 12$	$7.814e - 3$	$1.131e - 10$	$7.821e - 3$	$1.900e - 9$
IAE	$3.285e - 2$	1.056	$2.842e - 2$	3.494	$2.660e - 2$	$2.016e + 1$
POD-DO	$1.210e - 1$	$1.285e - 1$	$1.337e - 1$	$4.731e - 2$	$1.410e - 1$	$1.093e - 2$
GT	$3.744e - 2$	1.187	$3.902e - 2$	1.411	$3.848e - 2$	1.791

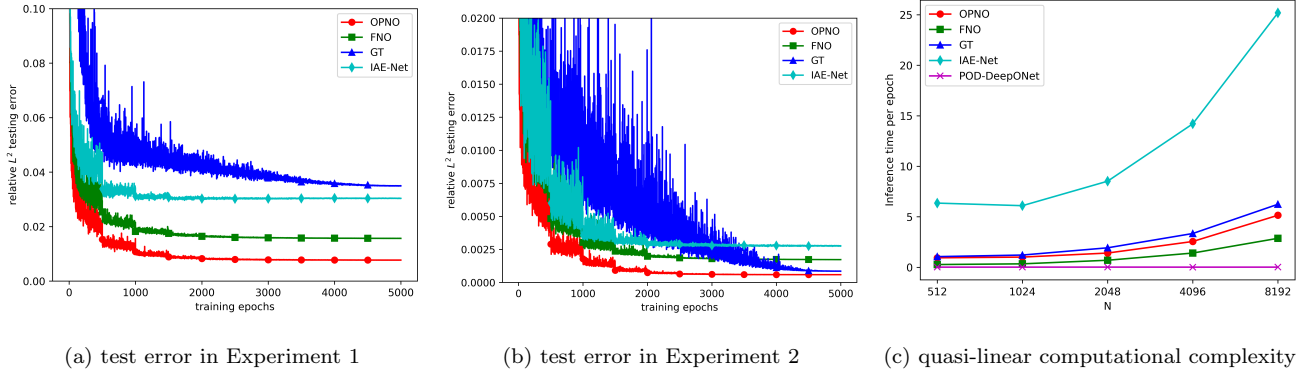


Figure 8: **The relative L^2 errors with respect to the number of training iterations** in Burgers-Neumann-BC experiment (a) and heat-Robin-BC experiment (b) with $N = 256$, where the neural operators exhibit non-overfitting capacities after long training periods. **The GPU time required per epoch** (c) in heat-Robin-BC experiment, where the batch sizes of all models are set as 20.

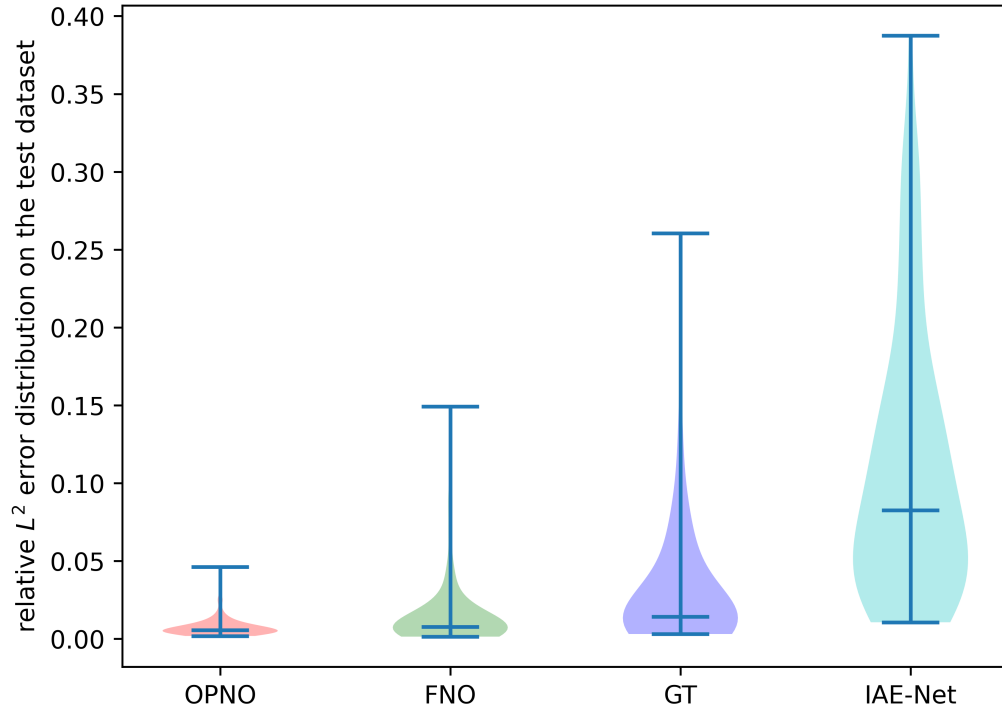


Figure 9: L^2 error distribution of the Burgers-Neumann-BC experiment.

4.2. Experiment 2: Heat diffusion equation with Robin BCs

When referring to the heat diffusion equation, the Robin BC is also known as the convection BC, which describes the convection heating/cooling occurring at an object’s surface and is crucial in many engineering fields, including the designs of chips and engines. Consider the equations

$$\partial_t u(x, t) - ku_{xx} + F(u, x) = 0, \quad x \in I, \quad (12)$$

$$u(x, 0) = u_0(x), \quad x \in I, \quad (13)$$

$$C_1 u(-1, t) - k_T u_x(-1, t) = C_2, \quad C_3 u(1, t) + k u_x(1, t) = C_4, \quad t \geq 0, \quad (14)$$

where k_T represents the conduction heat flux, and we are to investigate the approximation of $\mathcal{G} : \mathcal{G}(u_0(x)) = u(x, 1)$.

Furthermore, we remain curious about whether and how the test errors of neural operators can drop to significantly low levels in practice, but doubtlessly, a considerably large training dataset is helpful. To generate such a dataset (up to 10^6 training samples and 1000 test samples) using numerical methods, we fix the equation parameters $k_T = C_1 = C_3 = 0.02$, $C_2 = C_4 = 0$ and $F(u, x) \equiv 0$. To satisfy the BCs and provide the dataset with sufficient degrees of freedom, analogously to Eq. (11), the initial condition $u_0(x)$ is generated by a quasi-polynomial chaos expansion:

$$u_0(x) = \sum_{k=0}^{\infty} \hat{v}_k \phi_k(x) \xi_k,$$

where $\phi_k(x) = T_k(x) - \frac{k-1}{k+3} T_{k+2}(x)$ satisfies the Robin BC (14), and

$$\hat{v}_k = \frac{2\sigma}{\pi p_k} \gamma^{-k}.$$

We further set $\gamma = 1.1$, $\sigma = 4$, and $p_k = \tilde{c}_k + \left(\frac{k^2+1}{(k+2)^2+1}\right)^2$.

Comparison between deep learning methods: First, we perform an experiment on the sub-training set consisting of 1000 training instances, and the results are shown in table 3. Although the native OPNO seems to perform slightly worse than the GT, we note that the mini-batch strategy is important for neural operator training, and the OPNO overtakes the GT model once both models adopt the same batch size. Therefore, taking all factors into account, the OPNO obtains the lowest relative error among the tested models, and the output accurately satisfies the Robin BCs within machine precision. Predictions for three test instances are demonstrated in fig. 10, where the prediction and reference solutions coincide.

We also test the GPU time usage (seconds per epoch) required for training different models, and we can determine from fig. 8c that the OPNO model runs in quasi-linear time, whereas the POD-DeepONet is the fastest tested neural operator.

Comparison with the numerical method: Next, we compare OPNO with the traditional numerical method in terms of not only computational efficiency but also accuracy. Numerical methods with 2nd-order convergence are the most popular PDE solvers in scientific software due to their balance between efficiency and stability. To be precise, for Eq. (12), we adopt the centered second difference in the spatial direction and the second-order

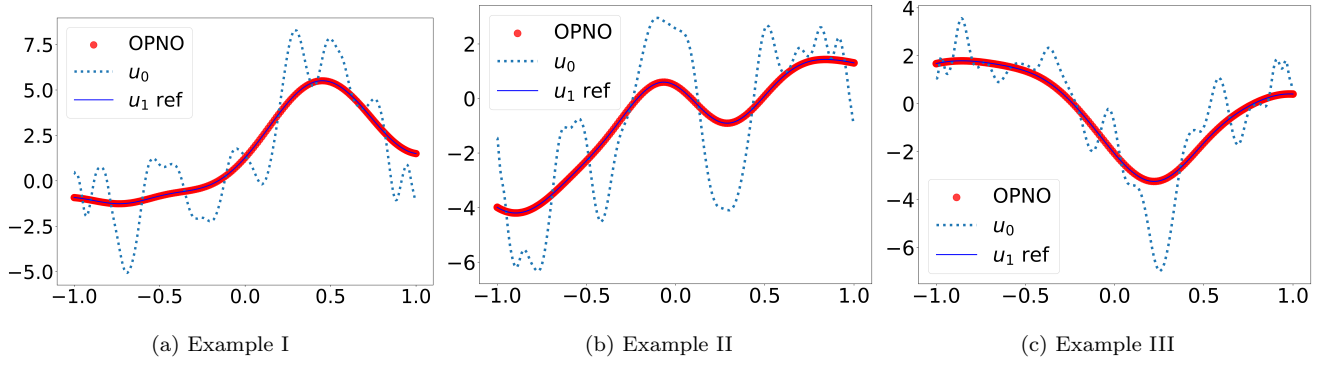


Figure 10: Evaluation results obtained by the OPNO for 3 test instances of the heat-Robin-BC experiment.

Table 3: Benchmarks on 1D heat equation with Robin BCs.

N	256		1024		4096	
	L^2	b.c. L^∞	L^2	b.c. L^∞	L^2	b.c. L^∞
FNO	$1.880e-3$	$6.030e-1$	$1.728e-3$	$8.394e-1$	$1.722e-3$	1.012
OPNO	$6.073e-4$	$2.325e-11$	$6.585e-4$	$4.595e-10$	$6.751e-4$	$7.055e-9$
IAE	$2.333e-3$	1.307	$1.618e-3$	2.485	$1.610e-3$	6.751
POD-DO	$4.052e-1$	$1.832e-1$	$4.156e-1$	$4.949e-2$	$4.084e-1$	1.956
GT ($bs = 4$)	$9.400e-4$	$5.634e-1$	$6.058e-4$	$9.203e-1$	$6.830e-4$	1.491
OPNO ($bs = 4$)	$2.927e-4$	$2.178e-11$	$2.423e-4$	$4.234e-10$	$2.843e-4$	$6.888e-9$

Crank–Nicolson method in the temporal direction, while the ghost point method is applied on the boundary to discretize the BCs (14). Let h and τ denote the spatial and temporal step sizes, respectively, and fix $h = \tau$. We recompute the 1000 test instances using this 2nd-order FDM, and the errors and the average time consumption levels obtained with different h, τ are listed in table 4. The results verify the 2nd-order convergence rate of FDM.

Note that system (12)–(14) is already one of the most trivial problems for the FDM to compute since only a sparse system of linear equations needs to be solved at each time step. As the mesh is refined, the discretization errors of the FDM decrease to an arbitrarily small value, but the computational cost also significantly increases. Nevertheless, the inference time of the OPNO is independent of the size of the training set, whereas the self-regularization feature suggests that the test errors of neural operators may reach desirably low levels once trained on a sufficiently large training set.

Consequently, we test the FNO and OPNO on sub-training sets with sizes ranging from 10^2 to 10^6 , and the relative L^2 errors are listed in table 5. A visual comparison chart against 2nd-order FDM is shown in section 4.2. The OPNO model has an inference time of only 3.75 ms compared to the 304,417 ms average computational time of the FDM and achieves a lower error than the 2nd-order FDM with a reasonably fine mesh possessing $h, \tau < 0.001$. While the results are already impressive, we emphasize that the error may be further reduced if better training techniques are employed. This also demonstrates the importance of choosing the correct underlying SOL basis that satisfies the given BCs.

Table 4: The average relative L^2 errors, numerical convergence order and time consumption (seconds) per instance of the **2nd-order FDM**.

h, τ	1/128	1/256	1/512	1/1024	1/2048
L^2 error	$1.091e-4$	$2.635e-5$	$6.563e-6$	$1.640e-6$	$4.101e-7$
order	–	2.050	2.005	2.001	2.0000
time (sec.)	0.0189	0.2294	2.192	32.634	304.417

Table 5: Relative L^2 errors induced by **neural operators** on training datasets with different sizes. $N = 256$, $bs = 20$.

training data	100	300	1000	3000
FNO	$8.858e-2$	$9.175e-3$	$1.880e-3$	$4.978e-4$
OPNO	$1.397e-2$	$3.964e-3$	$6.073e-4$	$8.509e-5$
training data	10000	30000	100000	
FNO	$2.412e-4$	$1.460e-4$	$1.382e-4$	
OPNO	$3.711e-5$	$3.054e-6(*)$	$1.124e-6(*)$	

(*) As the data size increases, the weight decay is set as 0, and each model is trained for 6000 epochs to mitigate underfitting.

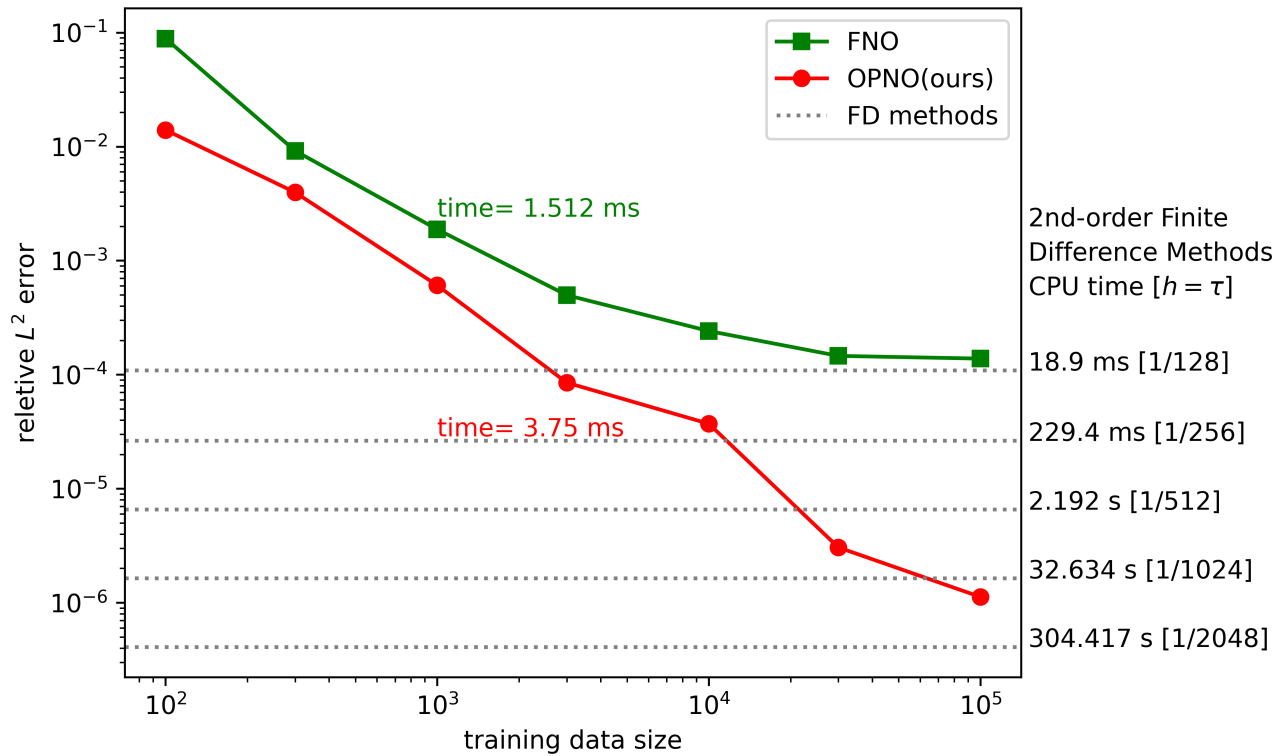


Figure 11: The inference times and relative L^2 errors of neural operators versus those of the 2nd-order FDM. For the neural operators, $N = 256$, and the batch size is set as 20.

4.3. Experiment 3: Heat diffusion equation with inhomogeneous Dirichlet BCs

Although solving PDEs with Dirichlet BCs is usually quite straightforward, this experiment aims to introduce a specific approach for solving PDEs with inhomogeneous BCs using the OPNO. Consider the approximation for the solution operator $S(1) : S(1)u_0 = u(x, 1)$ of the following heat diffusion equation with Dirichlet BCs:

$$\begin{aligned} \partial_t u(x, t) - k_T u_{xx} &= 0, \quad x \in I, \\ u(x, 0) &= u_0(x), \quad x \in I, \\ u(-1, t) &= a, \quad u(1, t) = b, \quad t > 0, \end{aligned} \tag{15}$$

with k_T set as 0.02. The above equations describe the heat conduction under the condition of constant surface temperature. The initial condition $u_0(x) = \Psi_0(x) + v_0(x)$ is generated according to $v_0 \sim \mu$, where $\mu = \mathcal{N}(0, 625(-4\Delta + 25I)^{-2})$ with homogeneous Dirichlet BCs, and

$$\Psi_0(x) = \frac{b-a}{2}x + \frac{a+b}{2}.$$

The BC parameters are fixed as $a = 0.3$, $b = -0.5$, and the dataset consists of 1000 training instances and 100 test instances.

Regarding the OPNO, the approach for satisfying the inhomogeneous BCs is to expand the basis. For the BCs (15), the polynomial basis is expanded to $\{\phi_k\}_{k \in \mathbb{N}} \cup \{\Psi_0\}$. The OPNO outperforms other neural operators, as shown in table 6. It is worth mentioning that the POD-DeepONet model automatically learns the Dirichlet BCs accurately.

Table 6: Benchmarks on 1D heat diffusion equation with inhomogeneous Dirichlet BCs.

N	256		1024		4096	
	L^2	b.c. L^∞	L^2	b.c. L^∞	L^2	b.c. L^∞
FNO	$2.402e-4$	$2.464e-4$	$2.364e-4$	$4.242e-4$	$2.360e-4$	$4.111e-4$
OPNO	$1.342e-4$	$1.363e-15$	$1.099e-4$	$1.356e-15$	$1.115e-4$	$1.362e-15$
POD-DO	$8.356e-3$	$6.351e-12$	$3.604e-2$	$2.145e-13$	$9.055e-2$	$5.069e-12$
IAE	$1.002e-3$	$7.265e-3$	$8.638e-4$	$7.203e-3$	$8.986e-4$	$9.416e-3$
GT	$5.877e-4$	$5.616e-4$	$5.931e-4$	$7.166e-4$	$6.149e-4$	$6.394e-4$

4.4. Experiment 4: 2D Burgers' equation with Neumann BCs

We consider the 2D Burgers' equation with Neumann BCs:

$$\partial_t u(x, t) + (u \cdot \nabla)u = \nu \Delta u(x, t), \quad x \in D$$

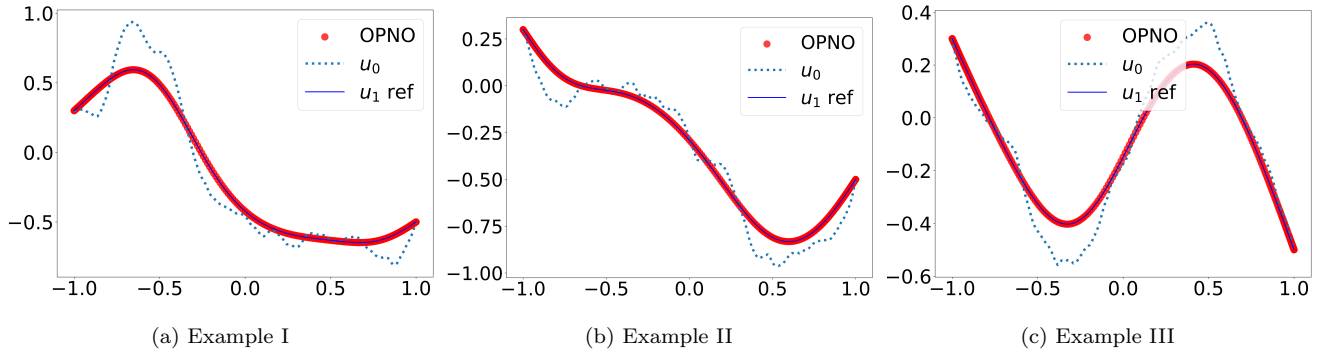


Figure 12: Evaluation results obtained by the OPNO for 3 test instances of the heat-Dirichlet-BC experiment.

subject to

$$\begin{aligned}
 u(x, 0) &= u_0(x), \quad x \in D, \\
 \frac{\partial u}{\partial \mathbf{n}}(x, t) &= 0, \quad x \in \partial D, \quad t > 0.
 \end{aligned}$$

where $D = I^2$. Rather than constructing a time-stepping recurrent solver, we are interested in learning the operator for directly mapping $u_0(x)$ to the set of solutions at a specific time $\{u(x, t_k)\}$, $t_k \in T$. We further fix $\nu = 0.001$ and $T = \{0.2, 0.6, 1\}$. The initial conditions are generated according to $u_0 \sim \mathcal{N}(0, 16(\Delta + 16I)^{-2})$ with homogeneous Neumann BCs.

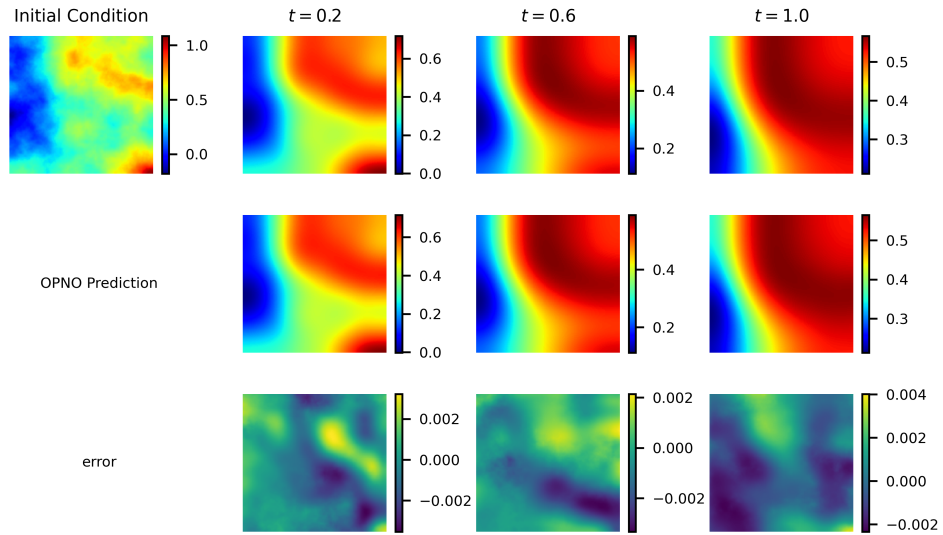
The FNO and OPNO models are trained for 3000 epochs with an initial learning rate 0.001 that is halved every 300 epochs, with their batch size fixed to 20. In addition, we deploy the neural operators with 16 modes and 24 channel width. table 7 shows that the OPNO also outperforms the FNO model in solving the 2d Burgers' equation, while two instances in test set for prediction is given in fig. 13.

Table 7: Benchmark results obtained on the 2D Burgers' equation with Neumann BCs.

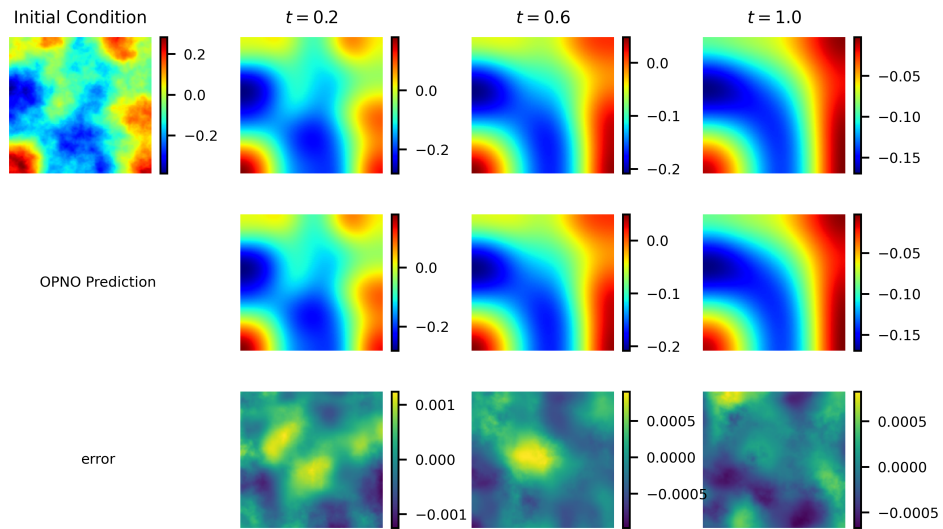
N	50		100		200	
	L^2	b.c. L^∞	L^2	b.c. L^∞	L^2	b.c. L^∞
FNO	$5.278e-3$	$1.625e-1$	$5.892e-3$	$3.590e-1$	$6.913e-3$	$7.849e-1$
OPNO	$3.714e-3$	$2.886e-12$	$3.359e-3$	$1.955e-12$	$3.354e-3$	$7.931e-12$

4.5. Discussions on the generalization errors

Based on the visualization of the training and test error landscapes, we aim to provide an intuitive explanation for the better performance and non-overfitting phenomena of OPNO. The training error landscape of the OPNO model for the Neumann-BC experiment (section 4.1) is demonstrated in fig. 14a, where the loss function is almost convex with respect to the learnable parameters θ_1 and θ_2 , making the OPNO easy to train. In addition, the contour plot about the comparison of the training and test error landscapes, along with its zoomed-in subgraph,



(a) Example I



(b) Example II

Figure 13: **Two OPNO prediction instances of 2D experiment** that are trained on 51×51 grids and tested on 201×201 grids. For each example, the upper figures are the reference solutions in the test data, while the middle figures are the predictions of the OPNO at the corresponding time based on the input initial condition, and the bottom row represents the pointwise errors of the OPNO predictions.

are demonstrated in fig. 14b and fig. 14c, respectively. One can see that the geometries of the two landscapes are pretty close.

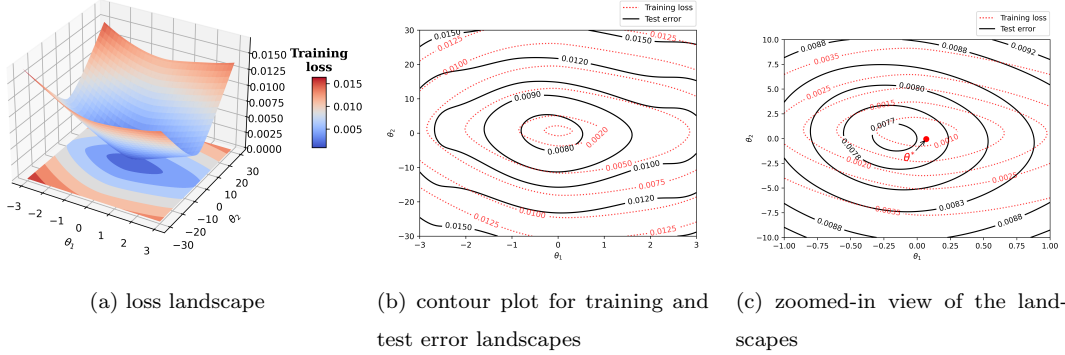


Figure 14: The training and test error landscapes of OPNO.

The similarity between the training and test error landscapes can result in the non-overfitting phenomena. Furthermore, it leads to a supervised model with low theoretical generalization error, which is usually decomposed into two components [22]: the “approximation error” (the minimum error achievable by the model in the hypothesis class, introduced by the model bias) and the “estimation error” (the difference between the approximation error and the minimum error achievable on the given data, depending on the size of the finite training data and the richness of hypothesis class).

While for one model, there is always a trade-off between these two errors (also known as the bias-variance trade-off), introducing the BC satisfaction architecture, however, can reduce both of them simultaneously. On the one hand, the approximation error is reduced by eliminating the model bias caused by wrong underlying function basis. On the other hand, the estimation error also decreases because the hypothesis space is limited to the class of operators with output strictly satisfying the BCs.

Moreover, the near-convex loss function enables the OPNO to practically obtained the achievable minimum error through long-term training. Consequently, as the result of the Robin-BC experiment (section 4.2) shows, if the size of the dataset is sufficiently large, the test errors of BC-satisfying neural operators can reach an impressively low level in practice.

5. Conclusion

In this study, based on the architecture of the Spectral Operator Learning, a boundary-condition-satisfying neural operator named Orthogonal Polynomial Neural Operator is proposed for solving PDEs with Dirichlet, Neumann and Robin BCs. As far as we are concerned, the OPNO is the first deep-learning method that can generate solutions strictly satisfying such non-periodic BCs for a family of PDEs, while extensive experiments verify that our model can

achieve the state-of-the-art performance in solving PDEs with these BCs. An analysis of the worst-case performance illuminates the key role of the BC satisfaction property in developing precise and reliable neural operators.

Based on a massive dataset, for the first time, we confirm that a deep-learning method can be more accurate in solving PDEs than a 2nd-order numerical method with a considerably fine mesh while being 4 to 5 orders of magnitude faster. The Universal Approximation Theorem is also provided, which ensures the expressive capacity of the proposed method.

Additionally, the OPNO model possesses other desirable computational properties: It is a fast algorithm with a time complexity of $O(N \log N)$, which is important for big-data training and large-scale predictions; models that are trained on a coarse mesh can be directly applied on a fine mesh without loss of numerical accuracy; and the model parameters are sparse and memory-efficient. These properties result from our adoption of the structure in spectral numerical methods for SOL architecture.

Appendix A. Chebyshev polynomials and their properties

According to the well-known Weierstrass approximation theorem, any continuous function $u(x) \in C(I)$ can be uniformly approximated by a polynomial function. Furthermore, the Chebyshev polynomials (of the first kind) form one of the most popular polynomials basis for developing numerical methods. They are given by the three-term recurrence relation

$$T_{n+1}(x) = 2xT_n(x) - T_{n-1}(x), \quad n \geq 1, \quad x \in I.$$

Fortunately, they have an explicit formula

$$T_n(x) = \cos n\theta, \quad \theta = \arccos(x), \quad x \in I,$$

from which we can easily derive the following properties:

$$\begin{aligned} T_n(\pm 1) &= (\pm 1)^n, \quad T'_n(\pm 1) = (\pm 1)^{n-1}n^n, \\ \int_{-1}^1 T_n(x)T_m(x) \frac{1}{\sqrt{1-x^2}} dx &= \frac{c_n\pi}{2} \delta_{mn} \\ T'(x) &= 2n \sum_{\substack{k=0 \\ k+n \text{ odd}}}^{n-1} \frac{1}{c_k} T_k(x), \end{aligned} \tag{A.1}$$

where $c_0 = 2$ and $c_n = 1$ for $n \geq 1$. Eq. (A.1) shows that the Chebyshev polynomials are orthogonal with respect to the weight function $\omega(x) = (1-x^2)^{-\frac{1}{2}}$, and thus for a given $N > 0$, the L_w^2 -orthogonal projection $\Pi_N : u(x) \mapsto \{\hat{u}_k\}_{0 \leq k \leq N}$ is defined as

$$\Pi_N(u)(x) \triangleq \sum_{k=0}^N \hat{u}_k T_k(x),$$

where

$$\hat{u}_k = \int_{-1}^1 u(x) T_k(x) \omega(x) dx.$$

Remark that the uniqueness of interpolation polynomials yields $I_N u = \Pi_N u$, $\forall u \in C(I)$.

Denote $\mathbb{P}_N(I)$ as the space of all polynomials on I of the degree no greater than N . For the CGL quadrature, the Chebyshev-Gauss-type nodes and weights are defined as

$$x_j = -\cos \frac{\pi j}{N}, \quad \omega_j = \frac{\pi}{c_j N}, \quad 0 \leq j \leq N,$$

where $c_j = 1$ for $j = 1, 2, \dots, N-1$ but $c_0 = c_N = 2$. As a consequence, the following equation holds:

$$\int_{-1}^1 p(x) \frac{1}{\sqrt{1-x^2}} dx = \sum_{j=0}^N p(x_j) \omega_j, \quad \forall p \in \mathbb{P}_{2N-1}.$$

What's more, the discrete Chebyshev transform

$$\mathcal{C}_h : \{u(x_j)\}_{0 \leq j \leq N} \mapsto \{\hat{u}_k\}_{0 \leq k \leq N}$$

can be carried out with $O(N \log N)$ operations via fast Fourier transform (FFT).

For $u(x) = \sum_{k=0}^N \hat{u}_k T_k(x) \in \mathbb{P}_N(I)$, its derivative $u' = \sum_{k=0}^{N-1} \hat{u}_k^{(1)} T_k(x)$ is obtained by performing differentiation on the frequency space, namely,

$$\begin{cases} \hat{u}_{N-1}^{(1)} = 2N \hat{u}_N, \\ \hat{u}_{k-1}^{(1)} = (2k \hat{u}_k + \hat{u}_{k+1}^{(1)}) / \tilde{c}_{k-1}, \quad k = N-1, \dots, 1, \end{cases} \quad (\text{A.2})$$

which can also be calculated via a linear convolution procedure in $O(N \log N)$ operations.

Appendix B. The fast compacting transform for Neumann conditions

For the compact combination $\phi_k(x) = T_k(x) - \frac{k^2}{(k+2)^2} T_{k+2}$ satisfying the BCs in Eq. (10), we have the **forward compacting transform**

$$\beta_j = \begin{cases} \alpha_j, & j = 0, 1, \\ p_j \beta_{j-2} + \alpha_j, & 2 \leq j \leq N-4, \\ -\frac{1}{p_j} \alpha_{j+2}, & j = N-3, N-2, \end{cases}$$

and the **backward compacting transform**

$$\alpha_j = \begin{cases} \beta_j, & j = 0, 1, \\ \beta_j - p_j \beta_{j-2}, & 2 \leq j \leq N-2, \\ -p_j \beta_{j-2}, & j = N-1, N, \end{cases}$$

where $p_{j+2} = j^2 / (j+2)^2$, $0 \leq j \leq N-2$.

Similarly, the only troublesome part when conducting parallel computing is the forward transform with $2 \leq j \leq N-2$. However, let $\tilde{\alpha}_j = j^2 \alpha_j$, $\tilde{\beta}_j = j^2 \beta_j$; then, we obtain the following equation:

$$\tilde{\beta}_j = \tilde{\beta}_j + \tilde{\alpha}_j, \quad 2 \leq j \leq N-2,$$

which can be efficiently computed with the linear convolution method. A similar approach can also be applied to the Robin BCs.

Appendix C. Proof of the Universal Approximation Theorem theorem 3.2

The constructive proof of the Universal Approximation Theorem for the FNO has been given in [9] by Nikola Kovachki, Samuel Lanthaler, and Siddhartha Mishra. Besides, Hao Liu, Haizhao Yang, et al. also estimated the generalization error of neural operators with encoders and decoders of trigonometric functions or Legendre polynomials in [12]. Actually, Jacobi's expansions [18] for the underlying basis of FNO show that

$$\begin{aligned}\sin(k\pi x) &= 2 \sum_{n=0}^{\infty} (-1)^n J_{2n+1}(k\pi) T_{2n+1}(x), \\ \cos(k\pi x) &= J_0(z) + 2 \sum_{n=1}^{\infty} (-1)^n J_{2n}(k\pi) T_{2n}(x),\end{aligned}$$

where $J_n(x)$ is the Bessel function of the first kind. Using the asymptotic formula

$$J_k(x) \sim \frac{1}{2k\pi} \left(\frac{ex}{2k} \right)^k, \quad k \gg 1,$$

we find that the expansion coefficients exponentially decay as long as N is sufficiently large. Therefore, one can guess from intuition that it should be feasible to extend the Universal Approximation Theorem to the OPNO model with finite modes and bandwidth.

Denote the L^2 norm $\|\cdot\|_{L^2}$ by $\|\cdot\|$ in short. Before we start the proof, as a result of the following lemma given in [9], we adjust the direction of the proof to approximating the ‘‘spectral projection’’ operator $\mathcal{G}_N \triangleq \Pi_N \mathcal{G}(\Pi_N a)$ instead of the original operator \mathcal{G} using neural operators:

Lemma Appendix C.1 ([9]). $\forall \epsilon > 0$, there exists $N \in \mathbb{N}$ such that

$$\|\mathcal{G}(a) - \mathcal{G}_N(a)\| \leq \epsilon, \forall a \in K.$$

lemma Appendix C.1 is a consequence of the following facts: Since $K \subset H^s(I^d)$ is compact and \mathcal{G} continuous, the set $\hat{K} \triangleq K \cup \bigcup_{N \in \mathbb{N}} \Pi_N K$ and its image $\mathcal{G}(\hat{K})$ are also compact, and $\mathcal{G}|_{\hat{K}}$ uniformly continuous. The compactness of $\mathcal{G}(\hat{K})$ gives the existence of a modulus of continuity $\omega : [0, \infty) \rightarrow [0, \infty)$, such that

$$\|\mathcal{G}(a) - \mathcal{G}(a')\| \leq \omega(\|a - a'\|_{H^s}), \quad \forall a, a' \in \hat{K},$$

while the compactness of both \hat{K} and $\mathcal{G}(\hat{K})$ yields

$$\limsup_{N \rightarrow \infty} \sup_{v \in \mathcal{G}(\hat{K})} \|(1 - \Pi_N)v\| = 0 = \limsup_{N \rightarrow \infty} \sup_{a \in \hat{K}} \|(1 - \Pi_N)a\|_{H^s}. \quad (\text{C.1})$$

So we have the inequality

$$\begin{aligned}\|\mathcal{G}(a) - \mathcal{G}_N(a)\| &= \|\mathcal{G}(a) - \Pi_N \mathcal{G}(\Pi_N a)\| \\ &\leq \|\mathcal{G}(a) - \Pi_N \mathcal{G}(a)\| + \|\Pi_N \mathcal{G}(a) - \Pi_N \mathcal{G}(\Pi_N a)\| \\ &\leq \sup_{v \in \mathcal{G}(\hat{K})} \|(1 - \Pi_N)v\| + \omega(\sup_{a \in \hat{K}} \|a - \Pi_N a\|_{H^s}) \\ &\leq \epsilon.\end{aligned}$$

holds once N is sufficiently large.

Thus, the problem reduces to constructing an OPNO that approximates \mathcal{G}_N . After defining an auxiliary operator $\hat{\mathcal{G}}_N$ such that

$$\mathcal{G}_N(a) = \mathcal{C}_h^{-1} \circ \hat{\mathcal{G}}_N \circ [\mathcal{C}_h \circ \Pi_N](a),$$

we now perform its individual steps, in which we set $d_a = d_v = d = 1$ without any loss of generalization.

Appendix C.1. Approximation of $\mathcal{C}_h \circ \Pi_N$ (the discrete Chebyshev transform)

The trick used in the proof is to manually build a discrete Chebyshev polynomial decomposition (or its inverse in the next subsection) in the **channel** dimension, even though in the structure of the OPNO, such a transform is performed in the spatial dimension. Please refer to fig. C.15 for the schematic diagram. Specifically, instead of

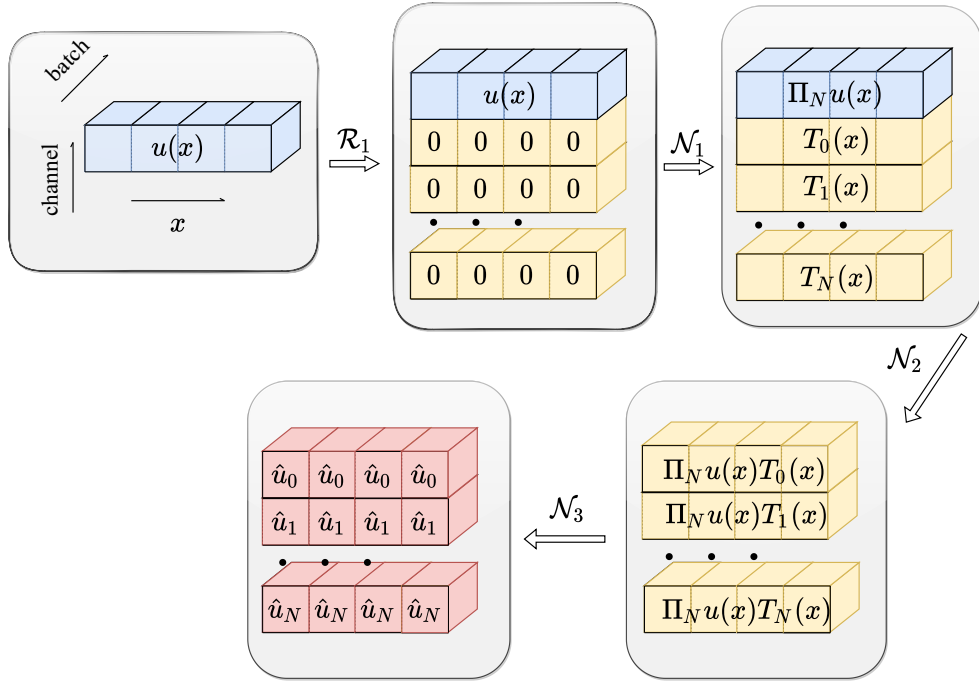


Figure C.15: Schematic diagram for the OPNO approximation of the operator $\mathcal{C}_h \circ \Pi_N$

an $(N + 1)$ -dimensional vector, we view the output of the target operator as a **constant $(N + 1)$ -dimensional vector-valued function**. In other word, we aim to approximate the operator

$$\mathcal{C}_h \circ \Pi_N : L^2(I; \mathbb{R}) \rightarrow L^2(I; \mathbb{R}^{N+1}), \quad v(x) \mapsto \hat{w}(x) \equiv \{\hat{v}_k\}_{k \in K_N},$$

where $K_N = \{0, 1, 2, \dots, N\}$ and \hat{v}_k is the k -th Chebyshev polynomial expansion coefficient of $v(x)$.

It is notable that the OPNO layer (Eq. eq. (7)) reduces to a vanilla (ResNet) neural network when filling all parameters of A_l with 0. In other words, feedforward neural networks can be seen as trivial instances of the OPNO. So we denote by $\mathbf{a} \vee \mathbf{b}$ the concatenation in the channel dimension of the two vectors herein, and define a lifting

operator \mathcal{R}_1 as well as two continuous operators $\mathcal{N}_1, \tilde{\mathcal{N}}_2$ such that

$$\begin{aligned}\mathcal{R}_1 &: L^2(I) \rightarrow L^2(I; \mathbb{R}^{N+2}), v(x) \mapsto w^{(0)}(x) \triangleq \{v(x)\} \vee \mathbf{0}_{N+1}, \\ \mathcal{N}_1 &: L^2(I; \mathbb{R}^{N+2}) \rightarrow L^2(I; \mathbb{R}^{N+2}), w^{(0)}(x) \mapsto w^{(1)}(x) \triangleq \left\{ \Pi_N w_0^{(0)} \right\} \vee \{T_k(x)\}_{k \in K_N}, \\ \tilde{\mathcal{N}}_2 &: L^2(I; \mathbb{R}^{N+2}) \rightarrow L^2(I; \mathbb{R}^{N+1}), w^{(1)}(x) \mapsto w^{(2)}(x) \triangleq \left\{ w_0^{(1)} \cdot w_{1+k}^{(1)} \right\}_{k \in K_N}.\end{aligned}$$

Therefore,

$$\tilde{\mathcal{N}}_2 \circ \mathcal{N}_1 \circ \mathcal{R}_1(v)(x) = \{\Pi_N v(x) \cdot T_k(x)\}_{k \in K_N}.$$

Notably, $\mathcal{N}_1(w^{(0)})(x) = b_1(x) + \mathcal{S}^{-1}(\mathcal{A}_1 \mathcal{C}_h w^{(0)})(x)$ is an OPNO layer with

$$b_1(x) = 0 \vee \{T_k(x)\}_{k \in K_N}, \quad \mathcal{A}_1 = \mathcal{C}_h \circ \mathbf{1}_{k \leq N},$$

and $\tilde{\mathcal{N}}_2$ is simply a multiplication operation that can be easily approximated by a σ -activated neural network \mathcal{N}_2 .

Furthermore, using the fact that

$$\mathcal{C}_h[w^{(2)}(\cdot)](j) = \mathcal{C}_h \left[\Pi_N v(\cdot) T_k(\cdot) \right](j) = \int_{-1}^1 \Pi_N v(x) T_k(x) T_j(x) w(x) dx$$

and plugging $j = 0$ back into the above equation, we find that

$$\mathcal{C}_h \left[\Pi_N v(\cdot) T_k(\cdot) \right](0) = \langle \Pi_N v(x), T_k(x) \rangle_w = \hat{v}_k.$$

In other words, letting $\mathcal{A}_3 = \mathcal{C}_p \circ \mathbf{1}_{k=0}$, we have

$$\mathcal{S}^{-1} \mathcal{A}_3 \mathcal{C}_h [\Pi_N v(\cdot) T_k(\cdot)] = \mathcal{C}_h^{-1} \{\hat{v}_k \vee \mathbf{0}_N\} = \hat{v}_k T_0(x) \equiv \hat{v}_k.$$

Consequently, we define an OPNO layer \mathcal{N}_3 such that

$$\mathcal{N}_3 : L^2(I; \mathbb{R}^{N+1}) \rightarrow L^2(I; \mathbb{R}^{N+1}), \tilde{w}^{(2)}(x) \mapsto w^{(3)}(x) \triangleq \mathcal{S}^{-1} \mathcal{A}_3 \mathcal{C}_h w^{(2)}.$$

Finally, let $\mathcal{L}_1 = \mathcal{N}_3 \circ \mathcal{N}_2 \circ \mathcal{N}_1 \circ \mathcal{R}_1$, then \mathcal{L}_1 is the desired answer. Broadly speaking, \mathcal{L}_1 is an OPNO ‘‘up to σ -activation’’ since the activation function is missing in \mathcal{N}_3 . Such a difference, however, is insignificant due to the flexibility of neural networks, especially in practical applications, and can always be fixed by composition with a σ -activated neural network approximating the identity.

Appendix C.2. Approximation of \mathcal{C}_h^{-1}

The operator \mathcal{C}_h^{-1} is seen as an operator with a constant vector-valued function $\hat{w}(x) \in L^2(I; \mathbb{R}^{N+1})$ as input, where

$$\hat{w}(x) \equiv \{\hat{w}_k\}_{k \in K_N}.$$

Let

$$\begin{aligned}\mathcal{R}_2 &: L^2(I; \mathbb{R}^{N+1}) \rightarrow L^2(I; \mathbb{R}^{2N+2}), \hat{w}(x) \mapsto \hat{w}^{(0)} \triangleq \hat{w}(x) \vee \{T_k(x)\}_{k \in K_N}, \\ \tilde{\mathcal{N}}_4 &: L^2(I; \mathbb{R}^{2N+2}) \rightarrow L^2(I; \mathbb{R}), \hat{w}^{(0)}(x) \mapsto w(x) \triangleq \sum_{k=0}^N \hat{w}_k^{(0)}(x) \cdot w_{k+N+1}^{(0)}(x).\end{aligned}$$

Then, we have

$$\tilde{\mathcal{N}}_4 \circ \mathcal{R}_2(\hat{w}(x)) = \sum_{k=0}^N \hat{w}_k T_k(x) = \mathcal{C}_h^{-1} \hat{w}(x).$$

Apparently, $\mathcal{R}_2(\hat{w}(x)) = W_4 w(x) + b(x)$ with

$$W_4 = \begin{bmatrix} \mathbf{E}_{(N+1) \times (N+1)} \\ \mathbf{0}_{(N+1) \times (N+1)} \end{bmatrix} \in \mathbb{R}^{(2N+2) \times (N+1)}, \quad b(x) = \mathbf{0}_{N+1} \vee \{T_k(x)\}_{k \in K_N},$$

and there exists a conventional neural network \mathcal{N}_4 approximating $\tilde{\mathcal{N}}_4$ to any desired accuracy. Consequently, the OPNO $\mathcal{L}_2 \triangleq \mathcal{N}_4 \circ \mathcal{R}_2$ is the desired answer.

Appendix C.3. Approximation of $\hat{\mathcal{G}}_N$

It remains to be shown that the operator $\hat{\mathcal{G}}_N$ can be approximated by an OPNO, which is straightforward since this operator is nothing but a continuous map between compact subsets of **finite**-dimensional function spaces. According to the Universal Approximation Theorem of feedforward neural networks, there exists a (degenerate) OPNO \mathcal{L}_3 that approximates \mathcal{G}_N to an arbitrary level of precision. Select the activation function σ as a Lipschitz function, then \mathcal{L}_3 is thus also Lipschitz continuous with a Lipschitz constant $\text{Lip}(\mathcal{L}_3)$.

Remind that the image of a compact set remains compact under any continuous function (operator), and any continuous function on a compact set attains its maximum. Following the processes above, for any fixed $\epsilon > 0$, we construct the OPNOs $\mathcal{L}_1, \mathcal{L}_2, \mathcal{L}_3$ such that the following equations hold for any compact set $K \subset H^s(I)$:

$$\begin{aligned} \text{Lip}(\mathcal{L}_3) \sup_{a \in K} \|(\mathcal{C}_h \Pi_N - \mathcal{L}_1)a\| &< \frac{\epsilon}{3 \|\mathcal{C}_p^{-1}\|}, \\ \sup_{w \in \mathcal{C}_h \Pi_N(K)} \|(\hat{\mathcal{G}}_N - \mathcal{L}_3)w\| &< \frac{\epsilon}{3 \|\mathcal{C}_p^{-1}\|}, \\ \sup_{v \in \mathcal{L}_3 \circ \mathcal{L}_1(K)} \|(\mathcal{C}_h^{-1} - \mathcal{L}_2)v\| &< \frac{\epsilon}{3}, \end{aligned}$$

where

$$\|\mathcal{C}_p^{-1}\| = \sup_{\hat{w}(x) \equiv \{\hat{w}_k\}_{k \in K_N}} (\|\mathcal{C}_p^{-1} \hat{w}(x)\| / \|\hat{w}(x)\|).$$

To summarize, let $\mathcal{L} = \mathcal{L}_2 \circ \mathcal{L}_3 \circ \mathcal{L}_1$, then

$$\begin{aligned}
\sup_{a \in K} \|\mathcal{G}_N a - \mathcal{L}a\| &= \sup_{a \in K} \left\| \mathcal{C}_h^{-1} \circ \hat{\mathcal{G}}_N \circ \mathcal{C}_h \Pi_N a - \mathcal{L}_2 \circ \mathcal{L}_3 \circ \mathcal{L}_1 a \right\| \\
&\leq \sup_{a \in K} \left\| \mathcal{C}_h^{-1} \circ \hat{\mathcal{G}}_N \circ \mathcal{C}_h \Pi_N a - \mathcal{C}_h^{-1} \circ \mathcal{L}_3 \circ \mathcal{L}_1 a \right\| \\
&\quad + \sup_{a \in K} \left\| \mathcal{C}_h^{-1} \circ \mathcal{L}_3 \circ \mathcal{L}_1 a - \mathcal{L}_2 \circ \mathcal{L}_3 \circ \mathcal{L}_1 a \right\| \\
&\leq \|\mathcal{C}_p^{-1}\| \sup_{a \in K} \left\| \hat{\mathcal{G}}_N \circ \mathcal{C}_h \Pi_N a - \mathcal{L}_3 \circ \mathcal{L}_1 a \right\| \\
&\quad + \sup_{v \in \mathcal{L}_3 \circ \mathcal{L}_1(K)} \left\| \mathcal{C}_h^{-1} v - \mathcal{L}_2 v \right\| \\
&\leq \|\mathcal{C}_p^{-1}\| \left(\sup_{a \in K} \left\| \hat{\mathcal{G}}_N \circ \mathcal{C}_h \Pi_N a - \mathcal{L}_3 \circ \mathcal{C}_h \Pi_N a \right\| \right. \\
&\quad \left. + \sup_{a \in K} \left\| \mathcal{L}_3 \circ \mathcal{C}_h \Pi_N a - \mathcal{L}_3 \circ \mathcal{L}_1 a \right\| \right) \\
&\quad + \sup_{v \in \mathcal{L}_3 \circ \mathcal{L}_1(K)} \left\| (\mathcal{C}_h^{-1} - \mathcal{L}_2) v \right\| \\
&\leq \|\mathcal{C}_p^{-1}\| \sup_{w \in \mathcal{C}_h \Pi_N(K)} \left\| (\hat{\mathcal{G}}_N - \mathcal{L}_3) w \right\| \\
&\quad + \|\mathcal{C}_p^{-1}\| \text{Lip}(\mathcal{L}_3) \sup_{a \in K} \left\| (\mathcal{C}_h \Pi_N - \mathcal{L}_1) a \right\| \\
&\quad + \sup_{v \in \mathcal{L}_3 \circ \mathcal{L}_1(K)} \left\| (\mathcal{C}_h^{-1} - \mathcal{L}_2) v \right\| \\
&< \epsilon,
\end{aligned}$$

which complete the proof.

References

- [1] S. CAI, Z. WANG, L. LU, T. A. ZAKI, AND G. E. KARNIADAKIS, *DeepM&Mnet: Inferring the electroconvection multiphysics fields based on operator approximation by neural networks*, Journal of Computational Physics, 436 (2021), p. 110296.
- [2] S. CAO, *Choose a Transformer: Fourier or Galerkin*, Advances in Neural Information Processing Systems, 34 (2021), pp. 24924–24940.
- [3] V. FANASKOV AND I. OSELEDETS, *Spectral Neural Operators*, arXiv preprint arXiv:2205.10573, (2022).
- [4] T. J. GRADY II, R. KHAN, M. LOUBOUTIN, Z. YIN, P. A. WITTE, R. CHANDRA, R. J. HEWETT, AND F. J. HERRMANN, *Towards large-scale learned solvers for parametric pdes with model-parallel fourier neural operators*, arXiv preprint arXiv:2204.01205, (2022).
- [5] G. GUPTA, X. XIAO, AND P. BOGDAN, *Multiwavelet-based operator learning for differential equations*, Advances in Neural Information Processing Systems, 34 (2021), pp. 24048–24062.

- [6] H. HUANG, JIANGUOWANG AND T. ZHOU, *An augmented lagrangian deep learning method for variational problems with essential boundary conditions*, Communications in Computational Physics, 31 (2022), pp. 966–986.
- [7] P. JIN, S. MENG, AND L. LU, *Mionet: Learning multiple-input operators via tensor product*, SIAM Journal on Scientific Computing, 44 (2022), pp. A3490–A3514.
- [8] P. JIN, Z. ZHANG, A. ZHU, Y. TANG, AND G. E. KARNIADAKIS, *Sympnets: Intrinsic structure-preserving symplectic networks for identifying hamiltonian systems*, Neural Networks, 132 (2020), pp. 166–179.
- [9] N. KOVACHKI, S. LANTHALER, AND S. MISHRA, *On universal approximation and error bounds for Fourier Neural Operators*, Journal of Machine Learning Research, 22 (2021), pp. Art–No.
- [10] H. LI, S. JIANG, W. SUN, L. XU, AND G. ZHOU, *A model-data asymptotic-preserving neural network method based on micro-macro decomposition for gray radiative transfer equations*, arXiv preprint arXiv:2212.05523, (2022).
- [11] Y. LIAO AND P. MING, *Deep Nitsche Method: Deep Ritz Method with Essential Boundary Conditions*, Communications in Computational Physics, 29 (2021), pp. 1365–1384.
- [12] H. LIU, H. YANG, M. CHEN, T. ZHAO, AND W. LIAO, *Deep nonparametric estimation of operators between infinite dimensional spaces*, arXiv preprint arXiv:2201.00217, (2022).
- [13] S. LIU, Z. HAO, C. YING, H. SU, J. ZHU, AND Z. CHENG, *A unified hard-constraint framework for solving geometrically complex pdes*, arXiv preprint arXiv:2210.03526, (2022).
- [14] L. LU, P. JIN, G. PANG, Z. ZHANG, AND G. E. KARNIADAKIS, *Learning nonlinear operators via deeponet based on the universal approximation theorem of operators*, Nature machine intelligence, 3 (2021), pp. 218–229.
- [15] L. LU, X. MENG, S. CAI, Z. MAO, S. GOSWAMI, Z. ZHANG, AND G. E. KARNIADAKIS, *A comprehensive and fair comparison of two neural operators (with practical extensions) based on fair data*, Computer Methods in Applied Mechanics and Engineering, 393 (2022), p. 114778.
- [16] L. LU, R. PESTOURIE, W. YAO, Z. WANG, F. VERDUGO, AND S. G. JOHNSON, *Physics-informed neural networks with hard constraints for inverse design*, SIAM Journal on Scientific Computing, 43 (2021), pp. B1105–B1132.
- [17] L. LYU, Z. ZHANG, M. CHEN, AND J. CHEN, *MIM: A deep mixed residual method for solving high-order partial differential equations*, Journal of Computational Physics, 452 (2022), p. 110930.
- [18] J. C. MASON AND D. C. HANDSCOMB, *Chebyshev polynomials*, Chapman and Hall/CRC, 2002.
- [19] Y. Z. ONG, Z. SHEN, AND H. YANG, *Integral autoencoder network for discretization-invariant learning*, Journal of Machine Learning Research, 23 (2022), pp. 1–45.

- [20] J. PATHAK, S. SUBRAMANIAN, P. HARRINGTON, S. RAJA, A. CHATTOPADHYAY, M. MARDANI, T. KURTH, D. HALL, Z. LI, K. AZIZZADENESHELI, ET AL., *Fourcastnet: A global data-driven high-resolution weather model using adaptive fourier neural operators*, arXiv preprint arXiv:2202.11214, (2022).
- [21] M. RAISSI, P. PERDIKARIS, AND G. E. KARNIADAKIS, *Physics-informed neural networks: A deep learning framework for solving forward and inverse problems involving nonlinear partial differential equations*, Journal of Computational physics, 378 (2019), pp. 686–707.
- [22] S. SHALEV-SHWARTZ AND S. BEN-DAVID, *Understanding machine learning: From theory to algorithms*, Cambridge university press, 2014.
- [23] J. SHEN, *Efficient spectral-Galerkin method II. Direct solvers of second-and fourth-order equations using Chebyshev polynomials*, SIAM Journal on Scientific Computing, 16 (1995), pp. 74–87.
- [24] J. SHEN, T. TANG, AND L.-L. WANG, *Spectral methods: algorithms, analysis and applications*, vol. 41, Springer Science & Business Media, 2011.
- [25] J. SIRIGNANO AND K. SPILIOPOULOS, *DGM: A deep learning algorithm for solving partial differential equations*, Journal of computational physics, 375 (2018), pp. 1339–1364.
- [26] L. N. TREFETHEN, *Spectral methods in MATLAB*, SIAM, 2000.
- [27] T. TRIPURA AND S. CHAKRABORTY, *Wavelet neural operator for solving parametric partial differential equations in computational mechanics problems*, Computer Methods in Applied Mechanics and Engineering, 404 (2023), p. 115783.
- [28] S. WANG, S. SANKARAN, AND P. PERDIKARIS, *Respecting causality is all you need for training physics-informed neural networks*, arXiv preprint arXiv:2203.07404, (2022).
- [29] C. WEN-HSIUNG, C. SMITH, AND S. FRALICK, *A fast computational algorithm for the discrete cosine transform*, IEEE Transactions on Communications, 25 (1977), pp. 1004–1009.
- [30] B. YU ET AL., *The Deep Ritz Method: A Deep Learning-Based Numerical Algorithm for Solving Variational Problems*, Communications in Mathematics and Statistics, 6 (2018), pp. 1–12.
- [31] K. ZHANG, Y. ZUO, H. ZHAO, X. MA, J. GU, J. WANG, Y. YANG, C. YAO, AND J. YAO, *Fourier neural operator for solving subsurface oil/water two-phase flow partial differential equation*, SPE Journal, (2022), pp. 1–15.
- [32] A. ZHU, P. JIN, AND Y. TANG, *Approximation capabilities of measure-preserving neural networks*, Neural Networks, 147 (2022), pp. 72–80.

- [33] L. ZONGYI, K. NIKOLA, A. KAMYAR, L. BURIGEDE, B. KAUSHIK, S. ANDREW, AND A. ANIMA, *Fourier Neural Operator for Parametric Partial Differential Equations*, in International Conference on Learning Representations, 2021.